**Article:**
Xu, Z, Seddon, JM, Beales, P orcid.org/0000-0001-9076-9793 et al. (2 more authors) (2021) Breaking Isolation to Form New Networks: pH-Triggered Changes in Connectivity Inside Lipid Nanoparticles. Journal of the American Chemical Society. ISSN 0002-7863

https://doi.org/10.1021/jacs.1c06244

# Breaking isolation to form new networks: pH-triggered changes in connectivity inside lipid nanoparticles

*Zexi Xu[1,3], John M. Seddon[2], Paul A. Beales[3], Michael Rappolt[1] and Arwen I.I. Tyler[1,*]*

[1] School of Food Science and Nutrition, University of Leeds, Leeds, LS2 9JT, United Kingdom.

[2]Department of Chemistry, Imperial College London, London W12 0BZ, United Kingdom.

[3]School of Chemistry and Astbury Centre for Structural Molecular Biology, University of Leeds, Leeds, LS2 9JT, United Kingdom.

**KEYWORDS** Lyotropic liquid crystals, hexosomes, micellosomes, pH-response, lipid nanoparticles, SAXS, cryo-TEM, stimuli-responsive.

**ABSTRACT**

There is a growing demand to develop smart nanomaterials that are structure-responsive as they have the potential to offer enhanced dose, temporal and spatial control of compounds and chemical processes. The naturally occurring pH gradients found throughout the body make pH an attractive stimulus for guiding the response of a nanocarrier to specific locations or (sub)cellular compartments in the body. Here we have engineered highly sensitive lyotropic liquid crystalline nanoparticles that reversibly respond to changes in pH by altering the connectivity within their structure at physiological temperatures. At pH 7.4, the nanoparticles have an internal structure consisting of discontinuous inverse micellar 'aqueous pockets' based on space group Fd3m. When the pH is ≤6, the nanoparticles change from a compartmentalized to an accessible porous internal structure based on a 2D inverse hexagonal phase (plane group p6mm). We validate the internal symmetry of the nanoparticles using Small Angle X-ray Scattering and cryogenic Transmission Electron Microscopy. The high resolution electron microscopy images obtained have allowed us for the first time to directly visualize the internal structure of the Fd3m nanoparticles and resolve the two different-sized inverse micelles that make up the structural motif within the Fd3m unit cell, which upon structural analysis reveal excellent agreement with theoretical geometrical models.

**TOC**

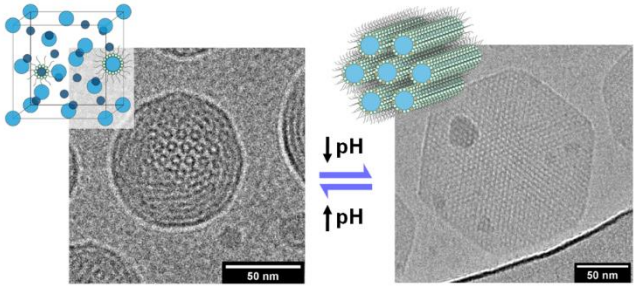


## INTRODUCTION

Lyotropic liquid crystalline nanoparticles (LCNPs) have attracted enormous interest for applications such as drug delivery, nanoreactor arrays, biosensors, templating, advanced biomaterials and functional foods. These particles have non-lamellar internal nanostructrures that possess two- or three-dimensional periodicity. LCNPs with internal nanostructures based on inverse bicontinuous cubics ($Q_{II}$), 2D-hexagonal ($H_{II}$) or ordered micellar phases are termed cubosomes, hexosomes and micellosomes respectively. They offer potential advantages over current nanoformulations, including favourable payloads due to their high internal surface area, simple preparation protocols, superior ease of conjugation with target biomolecules, biodegradability of the host building blocks and the ability to encapsulate hydrophobic, hydrophilic and amphiphilic substances.[1-6]

Currently there is a large demand to develop smart nanocarriers that can respond to particular environmental stimuli which could be used to release an active at a specific site of action and hence minimize off target toxicity and unwanted side effects. Extrinsic factors such as ultrasound, temperature, magnetic fields and light have been explored to trigger a response however these can only be controlled via external sources.[7] On the contrary, one can harness intrinsic stimuli such as

63 enzymes overexpressed at disease sites or variations in pH throughout the body, such as that found
64 in the stomach, or the more acidic extracellular microenvironment of tumor cells compared to
65 healthy tissue. [8-10] Acidic environments are also present in other organs/organelles such as the skin
66 surface where the pH is around 4-6.5,[11] <4 in the gastric phase,[12] and between 4.5-6.5 in the
67 lysosomal and endosomal lumen,[13] while the pH in the serum is 7.4. Acidic pH is also used *in vivo*
68 to trigger processes such as protein-ligand binding and viral fusion.[14]
69
70 Whilst the majority of pH responsive systems have been focused on polymers,[15-16] LCNPs are
71 mainly made up of biological amphiphiles rendering them more biocompatible and less cytotoxic.[6,
72 17-18] Non-lamellar forming lipids are some of the most common building blocks to generate inverse
73 lyotropic liquid crystalline phases as they can form a variety of structures depending on
74 composition, thermodynamic variables, pH and other parameters.[19-21] The resulting phase behavior
75 is also dependent on the geometric packing of the lipids and can be tuned by increasing the
76 concentration of more strongly curved lipids which will increase the negative spontaneous
77 curvature towards the water and form phases with increasing negative interfacial curvature.
78 (**Figure 1a**). A full range of inverse lyotropic lipid phase transitions with increasing amphiphile
79 concentration and increasing curvature can be seen in Kaasgaard and Drummond.[22] For example,
80 by increasing the fatty acid content in monoolein (MO) based systems, the structure can transform
81 from $Q_{II}$ to $H_{II}$ and on further addition to a discontinuous inverse micellar cubic phase of space
82 group Fd3m.[23-25] In an analogous fashion, the phase behavior can be tuned by introducing ionisable
83 lipids where the lipid headgroup can be protonated or deprotonated depending on the pH and ionic
84 strength. An increase in surface charge density will cause electrostatic repulsion between
85 headgroups, an increase of the effective headgroup area and consequently a decrease in the

magnitude of the spontaneous inverse curvature and the adoption of less curved phases (**Figure 1a**). Similarly, an increase in ionic strength will enhance charge screening and hinder the transition to less curved structures. Tuning the phase behavior of these systems is attractive as the release rate of encapsulated actives from LCNPs strongly correlates with the internal nanostructure symmetry as well as, for some LCNPs, the geometry and dimensions of their pores.[10, 26-27]

Most studies have focused on pH-induced transitions between lamellar (Lα) and $Q_{II}$, or between $Q_{II}$ and $H_{II}$ phases. A MO: linoleic acid system was developed to change from $Q_{II}$ at pH 7 to $H_{II}$ at pH 2 to simulate intestinal and gastric phases respectively.[28] Negrini *et al*. further developed a monolinolein: pyridinylmethyl linoleate system that switched from an $H_{II}$ to a $Q_{II}$ phase when the pH was ≤ 5.5 and showed the potential therapeutic role of this targeted system in treating cancer cells by exploiting their more acidic microenvironment.[29] A low pH-induced Lα to $Q_{II}$ phase transition in a MO: dioleoylphosphatidylserine system showed that the Lα phase directly transformed into an $H_{II}$, and subsequently, the $H_{II}$ slowly converted into a $Q_{II}$ phase.[30]

On the contrary, pH-triggered transitions from ordered inverse micellar phases is still in its infancy. These have an internal structure consisting of discontinuous micellar 'pockets' and, unlike the porous $Q_{II}$ and $H_{II}$ phases, these are based on a discontinuous packing of inverse micelles, containing an array of individual nanoscale aqueous compartments separated by fluid hydrophobic regions, which could potentially offer containment control.

Salentinig *et al.* showed that by increasing the pH from 6.8 to 9 at 25 °C in MO: oleic acid (OA) dispersions, an inverse micellar solution transformed to Fd3m micellosomes, to hexosomes, to cubosomes and finally to liposomes.[31] Similar phase transitions from LCNPs of OA doped with the antimicrobial human cathelicidin LL-37 peptide were observed upon increasing the pH from 6 to 8 at 25 °C.[32] Recently Fong *et al.* showed that at a certain MO: fatty acid composition Fd3m

micellosomes were formed in water with a pH of 4.9 and very low ionic strength. When water was replaced by PBS (pH 7.4) the micellosomes transformed to hexosomes at 30 °C. This transition was however triggered by the combination of pH and ionic concentration changes, and thus cannot be considered a pure pH response.[33]

In this work we aim to develop LCNPs that are switchable between the confined Fd3m and porous $H_{II}$ phases at physiologically relevant temperature and pHs, confirmed with detailed structural characterization by SAXS and cryo-TEM. We designed pH-responsive LCNPs based on MO and oleyl alcohol (Olalc) doped with a small amount (3 mol%) of a pH-sensitive lipid. We show that these LCNPs transform from Fd3m micellosomes at pH 7.4 to hexosomes when the pH is ≤ 6. To the best of our knowledge this is the first report of a pH triggered LCNP transition from Fd3m micellosomes to hexosomes with decreasing pH and compared to previous research on similar transitions, our system can reversibly transform at both room (25 °C) and at a biologically-relevant temperature (37 °C). We highlight that high resolution cryo-TEM images have allowed us to directly visualize the internal structure of the Fd3m nanoparticles with unprecedented detail allowing us to compare the internal structures of the nanoparticles with theoretical predictions, using cryo-TEM for this purpose for the first time.

## RESULTS AND DISCUSSION

### Phase behavior of oleyl alcohol, monoolein and DOBAQ mixtures reveal an $H_{II}$ to Fd3m transition

The phase diagram of MO in water has been widely studied;[34-35] above the excess water point of 35 wt%, MO adopts a Pn3m bicontinuous cubic phase between approximately 20 and 80 °C, which then transforms to an inverse hexagonal ($H_{II}$) phase at higher temperatures. Generally, for the other

pure component systems, DOBAQ forms liposomes in excess water,[36] whereas oleyl alcohol adopts an inverse micellar solution.[26]

The phase behavior of MO with fatty acids, such as oleic acid (OA), has previously been reported: MO:OA dispersions, stabilized by the Pluronic F127 in water, typically require an excess of 50 mol% OA to form Fd3m micellosomes,[31, 33] and when MO:OA dispersions are made in PBS at pH 7 and 100 mM NaCl (above the $pK_a^{app}$ of OA and hence the OA is negatively charged), over 80 mol% oleic acid is required to form the Fd3m phase.[37]

Here, we have chosen to study mixtures of monoolein with oleyl alcohol, which is structurally similar to OA but is not ionisable, doped with a small amount of the pH-sensitive lipid N-(4-carboxybenzyl)-N,N-dimethyl-2,3- bis (oleoyloxy) propan-1-aminium (DOBAQ). DOBAQ is neutral at physiological pH and becomes cationic as the pH is lowered, with a $pK_a$ of approximately 6 when measured in DOPC:DOBAQ 3:1 liposomes.[36] Preliminary exploration of the phase behavior of MO:Olalc:DOBAQ mixtures found that 3 mol% DOBAQ was optimal to reproducibly switch between the Fd3m and $H_{II}$ phases by lowering the pH. The phase behavior and lattice parameter ($a$) dependence of MO:Olalc dispersions at a fixed 3mol% DOBAQ at 25 and 37 °C and pH 7.4 are shown in **Figure 1b**. At this fixed DOBAQ ratio the system forms hexosomes between 37 and 39 mol% Olalc. Increasing Olalc to 41 mol% at 37 °C or 42 mol% at 25 ° C transforms the system to Fd3m micellosomes, with a small area of phase coexistence between 40 and 41 mol% Olalc at 25 °C and 40 mol% at 37 °C.

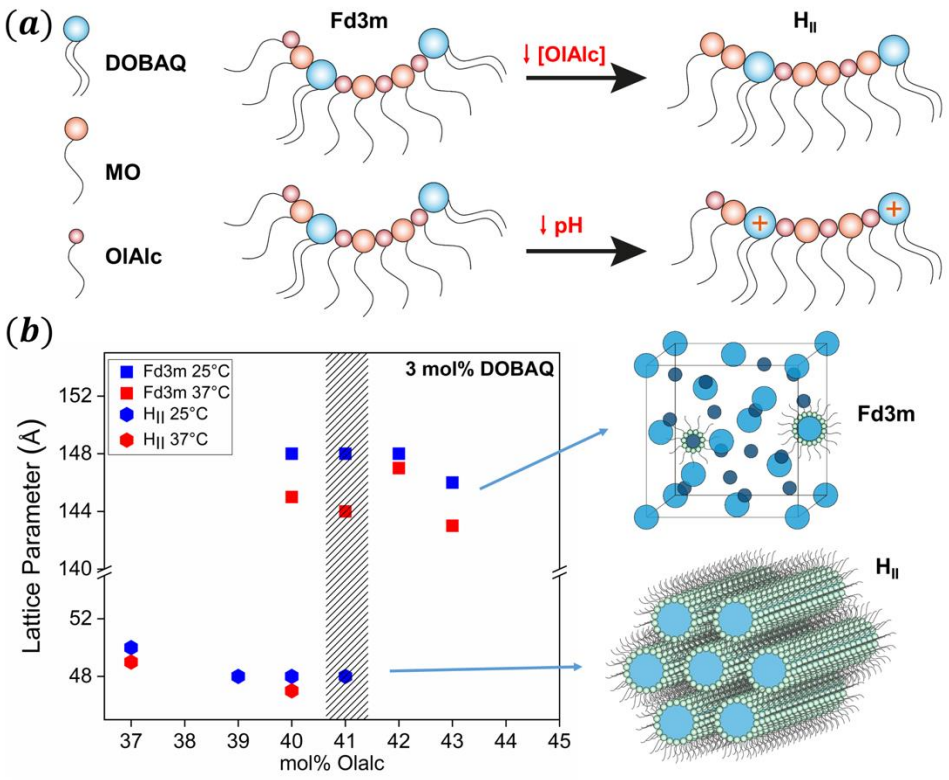


**Figure 1**. Design parameters to tune the negative interfacial curvature of the nanoparticles. (a) Increasing the amount of the weakly polar ampliphile OlAlc should drive the formation of more curved structures (top). Lowering the pH will cause DOBAQ to become cationic, increase its effective headgroup area and electrostatic repulsion between headgroups which should result in the adoption of less curved phases (bottom). (b) Phase behavior and the effect on the lattice parameter of incorporating Olalc into MO dispersions, keeping the pH sensitive lipid DOBAQ concentration fixed at 3 mol% in all samples at pH 7.4. The dashed region on the graph highlights the composition that was further studied as a function of pH.

Olalc is non-ionisable and has a slightly smaller headgroup compared to OA and hence lower concentrations are required to promote the Fd3m phase. This can be rationalized by increasing the magnitude of the spontaneous inverse monolayer curvature ($H_0$) towards water,[38] which is related to the structural parameters of the lipids as dictated by the critical packing parameter (CPP) in equation (1).

$$CPP = \frac{v}{a_o l} \quad (1)$$

where $v$ is the molecular volume of the fluid hydrocarbon chain(s), $l$ is the length of a fully extended hydrocarbon chain and $a_o$ is the interfacial area per molecule at the polar-non-polar interface.

Increasing Olalc concentration will decrease the headgroup area driving the formation of structures with increased negative curvature. This is evident in **Figure 1b** where an increase in Olalc causes a transition from hexosomes to the more inversely curved Fd3m micellosomes. Within the pure phase regions a reduction in the lattice parameters of both phases is observed, which is explained by the reduction in water concentration with increasing mean inverse interfacial curvature.

These nanoparticles were engineered and envisioned for future *in vitro/vivo* applications. Consequently, a composition that formed Fd3m micellosomes at physiological temperature was chosen to further study the nanoparticle phase behavior as a function of pH. MO:Olalc:DOBAQ (56:41:3 mol%) was selected as it lies very close to the phase boundary, making it easier to trigger structural transitions between the two phases by changing the pH. The size distribution of the nanoparticles at this selected composition was determined by DLS and cryo-TEM (**Figure 3**) and is described in the cryo-TEM section later.

**Fd3m to $H_{II}$ transitions can be triggered by decreasing pH at fixed composition**

The pH dependent phase behavior as determined by SAXS shows that F127 stabilized MO:Olalc:DOBAQ (56:41:3 mol%) dispersions clearly undergo phase changes in response to pH and demonstrates that the designed system can be tuned to switch between the Fd3m and $H_{II}$ phases (**Figure 2a**). In these experiments, MO:Olalc:DOBAQ dispersions were originally prepared at pH 7.4, aliquots taken and their pH subsequently adjusted by HCl.

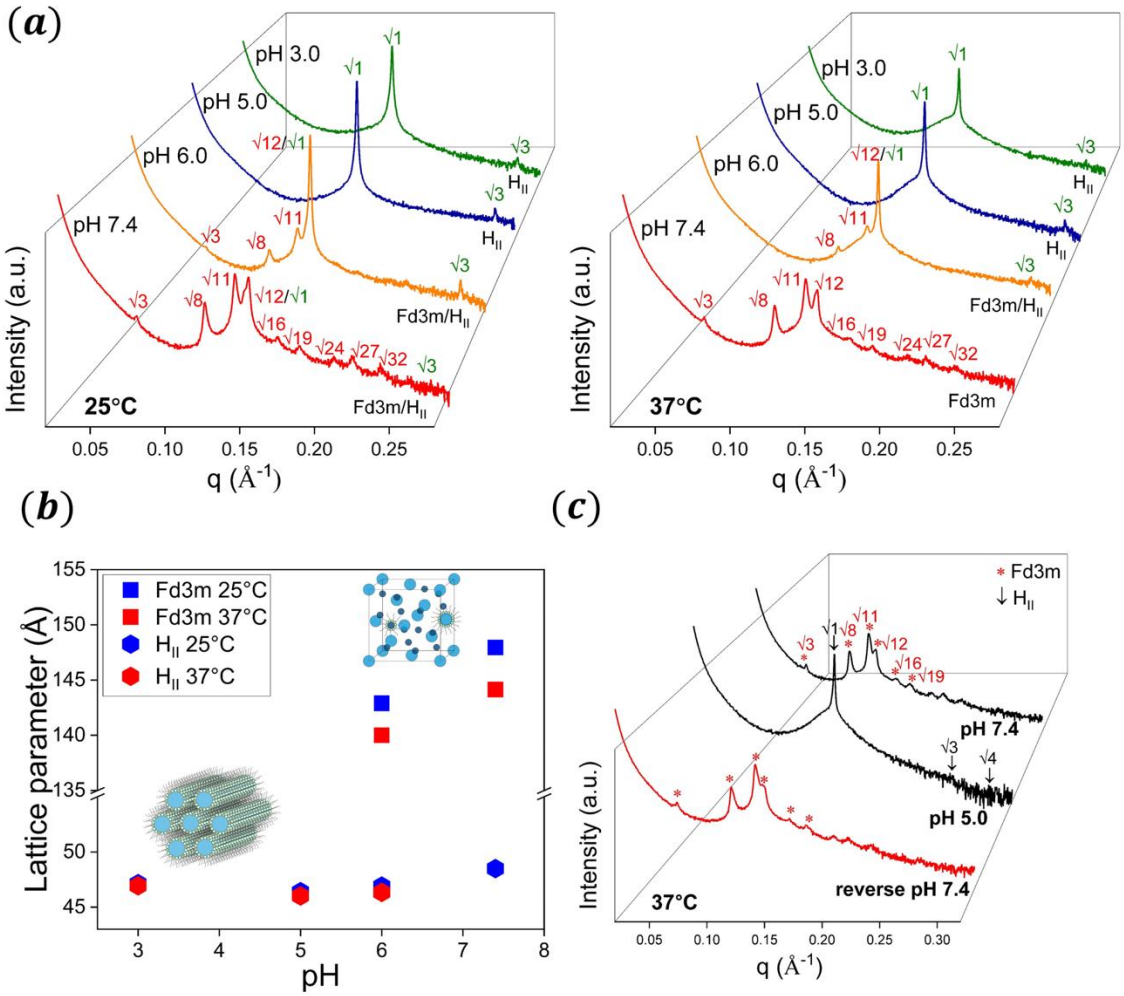


**Figure 2.** Fd3m to $H_{II}$ transitions can be triggered by decreasing pH and are fully reversible. (a) SAXS patterns of the 5 wt% F127 stabilized 56:41:3 mol % MO:Olalc:DOBAQ nanoparticles in PBS as a function of pH at 25 °C (left) and 37 °C (right). At pH 7.4, nine Bragg peaks are observed in the ratios of √3:√8: √11:√12:√16:√19:√24:√27:√32 (corresponding Miller indices (hkl) are 111, 220, 131, 222, 400, 331, 422, 333/511 and 440), which index as cubic space group *Fd3m* (red label). At 25°C, the Fd3m phase coexists with a small amount of a 2D inverse hexagonal phase ($H_{II}$). At pH 6.0, the system adopts an $H_{II}$ phase (green label), with a Bragg peak spacing ratio of √1: √3 (Miller indices (hk) are 10 and 11) indexing to plane group p6mm, coexisting with a small amount of Fd3m phase. When the pH is ≤ 5.0, only $H_{II}$ peaks were observed so the micellar cubosomes have completely transformed to hexosomes. (b) Phase behavior and effect on the lattice parameter of the nanoparticles as a function of pH. The lattice parameters of Fd3m phase decrease with the lowering of pH from 7.4 to 6.0 at both temperatures, then the Fd3m completely transforms to an $H_{II}$ phase when the pH is 5.0. (c) Reversible structural transitions triggered by pH at 37 °C: the pH of the dispersion was decreased from 7.4 to 5.0 (black curve) using HCl and then increased back to 7.4 (red curve) using NaOH. Indexing of the Fd3m (only the first 6 reflections are indexed for clarity) and the $H_{II}$ Bragg peaks are marked with red stars and black arrows respectively. There

is no significant change in the lattice parameter of the Fd3m phase and no additional phases were observed before and after the pH switch, highlighting that the transition is fully reversible.

At physiological pH, the system forms Fd3m micellosomes whereas at acidic pH the nanoparticles transform to hexosomes. This is attributed to the pH-sensitive behavior of DOBAQ, which is neutral at pH 7.4 due to a quaternary amine present in its headgroup and becomes cationic at acidic pH via protonation of its carboxylate group. The protonation of DOBAQ imposes a change in CCP, due to an increase in the surface charge density and enhanced electrostatic repulsion between charged headgroups. This in turn, increases the effective headgroup area and hence decrease the magnitude of the monolayer spontaneous inverse curvature driving the formation of less negatively curved phases.[2, 6, 39]

**Figure 2b** shows the variation in the structure and lattice parameter of the system with pH and temperature. At 25 °C and pH 7.4, the system adopts an Fd3m phase with a lattice parameter of 148 Å. An additional weak reflection occurring around $q \approx 0.15$ Å$^{-1}$ is due to a coexisting $H_{II}$ phase with a lattice parameter of 48 Å. At 37 °C and pH 7.4 the system adopts a pure Fd3m phase with a lattice parameter of 145 Å. Upon decreasing the pH from 7.4 to 6.0, the system transforms to hexosomes. This is supported by recording the characteristic √3-reflection of the $H_{II}$ phase (**Figure 2a**) with a small contribution of coexisting Fd3m micellosomes at both 25 and 37 °C. We note that diffraction peak intensities scale with the underlying material's volume fraction. Peak intensities can therefore be used to estimate the amount of material adopted by each respective phase. This transition is in agreement with the $pK_a$ of DOBAQ measured by Walsh *et al.* in a liposomal formulation ($pH \approx 6.0$).[36] Although the apparent $pK_a$ of a lipid has been shown to give rise to a distribution of $pK_a$ values that is dependent on the curvature and the phase adopted,[31] our results in Figure 2a are in line with the $pK_a$ estimate for DOBAQ reported by Walsh *et al*.[36] We further

note, that the Bragg peaks of the Fd3m phase shift to higher $q$ from pH 7.4 to 6, corresponding to a decrease in $a_{Fd3m}$ to 140 Å and 142 Å at 25 °C and 37 °C respectively. The effect of increasing temperature, which will increase the chain splay and $H_0$ resulting in a decrease in the lattice parameter of a mesophase, is consistent with the behavior seen here and with most lyotropic liquid crystalline formulations. On the contrary, the observation of a decrease in lattice parameter with an increase in charge is at first instance counter-intuitive, because an increase in charge should reduce $H_0$ and hence cause the lattice parameter of the Fd3m phase to increase. This trend could be rationalized by considering the size of the nanoparticles which is also highlighted in the subsequent section on cryo-TEM data. As seen in **Figures 3** and **4**, Fd3m micellosomes have a range of sizes and vary in their lattice parameters, with smaller nanoparticles generally displaying bigger lattice parameters and larger nanoparticles displaying smaller lattice parameters. The larger nanoparticles offer a bigger confinement volume for lyotropic liquid crystals to form, and as a consequence are less prone to structural defects and repulsive membrane undulation forces which will result in smaller lattice spacings and also render them more stable. We hypothesize that at pH 6, close to the pKa of DOBAQ, the weak reflections from the Fd3m structure are due to a few remaining more stable, relatively bigger Fd3m nanoparticles which have smaller lattice parameters (**Figure 2b)**. Within the timescale of the experiments presented here, by the time the nanoparticles were mixed with acid or base, loaded in a sample holder and a SAXS pattern collected (15 minutes or less), the nanoparticles had already switched their structure, giving an upper limit to the response time for structural switching in these nanoparticles.

At pH 5.0, only the $H_{II}$ phase was observed and hence the system has completely transformed from the initial Fd3m phase. Further decreasing the pH to 3 did not alter the phase behavior and the lattice parameter of the $H_{II}$ phase varied little (maximum ±2 Å) across all pH values measured.

**pH-triggered Fd3m to $H_{II}$ transitions are reversible**

To evaluate the potential to reverse the structural transition in the designed system at 37 °C, the pH of the sample was first lowered from pH 7.4 where the system adopted a pure Fd3m phase, to pH 5.0, where only the $H_{II}$ phase was observed. The pH was then subsequently raised back to 7.4 in the same sample leading to the reformation of the Fd3m phase. SAXS data demonstrate the reversibility of the Fd3m to $H_{II}$ transition by adjusting the pH of the PBS dispersions with NaOH or HCl (**Figure 2c**). The lattice parameter of the sample in the Fd3m phase before (144.9 Å) and after reversing the pH back to pH 7.4 (147.1 Å) is very similar, highlighting the truly reversible responsiveness of the system. The structure reversibility of the system is due to the protonation and deprotonation of the DOBAQ headgroup. When the pH is 7.4, the DOBAQ headgroup deprotonates and becomes neutral whereas at lower pH protonation causes the headgroup to become cationic. Repulsions between the gradually protonating or deprotonating carboxylic group of 3 mol% DOBAQ embedded at the lipid-water interface, modifies the system's spontaneous curvature.

MO can hydrolyze over long periods of time, producing oleic acid and glycerol[40] and the apparent $pK_a$ of oleic acid in MO:OA dispersions has been measured to be between 6-7.[31] Even if a small amount of MO has hydrolyzed, it has an insignificant effect on the phase transition as a.) samples consistently and reversibly switch between the Fd3m and $H_{II}$ phases at different pH values, indicating a true equilibrium phase behavior and b.) if instead a moderate amount of OA was

present, then this would cause the system to transform to an $H_{II}$ phase at pH 7.4 due to OA having a negative charge, leading to a decrease in curvature, and it would also hamper the formation of an $H_{II}$ phase at low pH due to being neutral, promoting more curved interfaces, such as in the Fd3m. This phase behavior is the exact opposite to what we observe here, so we conclude that Fd3m to $H_{II}$ transition at low pH is clearly dominated by the protonation/ deprotonation of the DOBAQ headgroup.

Note that both the $H_{II}$ and Fd3m phases have significant chain packing frustration, which might be thought to potentially lead to an out of equilibrium trapping of one or other of these phases. For example, during temperature jumps on MO dispersions, Dong *et al.*[41]showed supercooling effects as well as non-equilibrium structures appearing for more than thirteen hours before they returned to the equilibrium structure. As mentioned above, such effects are not seen here and we estimate our pH induced transitions to occur on the minute timescale based on our experimental observations and our previous studies of hydrostatic pressure induced Fd3m-$H_{II}$ phase transitions in similar lipid systems.[42]

The nanostructure of the designed system can be easily tuned by only a very small amount of pH-sensitive lipid, and shows the excellent pH sensitivity and selectivity of this system compared to previous studies where large amounts of ionisable lipids were required to switch between these two structures and/or significant changes in ionic strength of the buffer. Moreover, whilst an Fd3m to $H_{II}$ transition has been reported in the literature by increasing pH (although none have demonstrated this at 37 °C), this is the first example of an Fd3m to $H_{II}$ transition from physiological to acidic pH. This transition could potentially be advantageous in nanomedicine, where a hydrophilic active could be encapsulated into the inverse micelles of the Fd3m phase significantly hindering its release in the serum, but by rearranging to a porous $H_{II}$ phase, e.g. in the endosome,

can facilitate release. As an example, the diffusion coefficient of glucose from a system adopting the $H_{II}$ phase was shown to be approximately 15 times that observed in the Fd3m phase in bulk mesophases however how this translates to LCNPs is not known.[27]

By varying the position of the Gibbs-dividing surface to be between 13-15Å (see **Supporting Information** Section 1) we estimate the diameters of the small and big micelles to be between 22.7-26.7 and 34.5-38.5 Å respectively. Consequently, any hydrophilic molecule or globular protein with a diameter of up to 26.7 Å can be fully encapsulated into the Fd3m micellosomes and any molecule with a diameter of up to 38.5 Å can be partially incorporated into the big micelles of the Fd3m structure.

**Cryogenic Transmission Electron Microscopy (Cryo-TEM) facilitates quantitative structural characterization of individual LCNPs**

The cryo-TEM images of the designed MO:Olalc:DOBAQ 56:41:3 mol% system confirmed the pH-triggered nanostructural transitions observed by SAXS. At pH 7.4, the cryo-TEM image indicates the presence of Fd3m micellosomes coexisting with as small amount hexosomes, with the Fd3m micellosomes dominating in the dispersions (**Figure 3a**) at 25 °C. By contrast, only hexosomes were observed at pH 5.0 (**Figure 3b**).

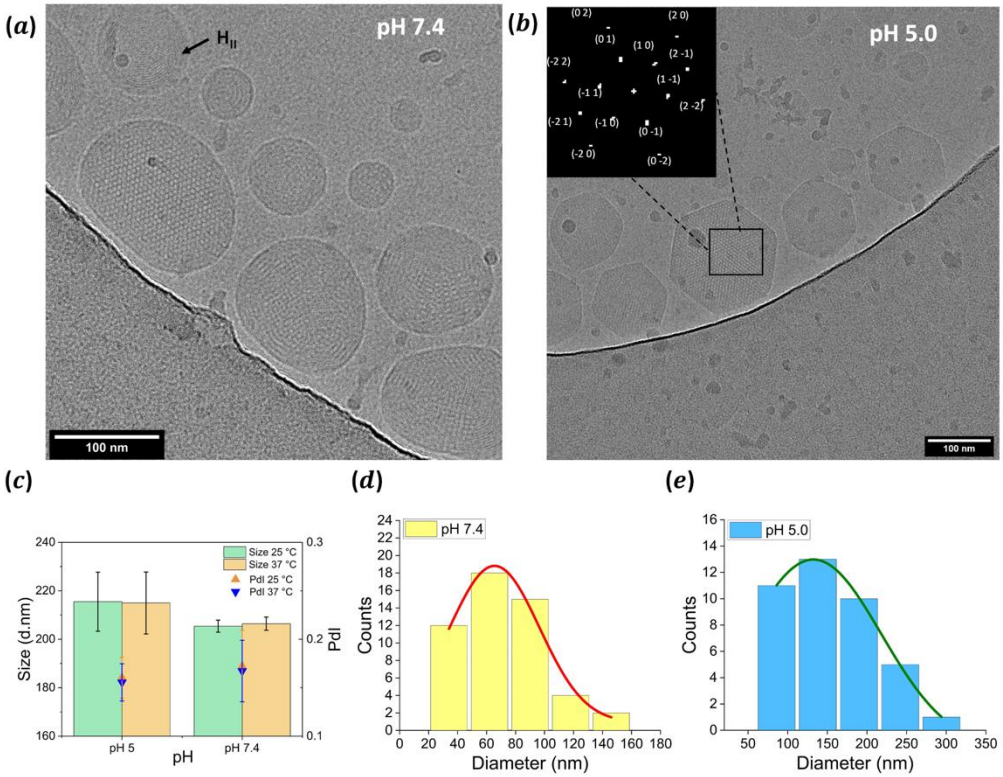


**Figure 3.** Representative cryo-TEM images of the MO:Olalc:DOBAQ 56:41:3 mol% system prepared at 25 °C and their size distributions. ($a$) Fd3m micellosomes at pH 7.4 coexisting with a small amount of hexosomes (black arrow), which likely give rise to the weak intensity of the √1 peak in the SAXS data in Figure 2$a$. Both SAXS and cryo-TEM data are in agreement that the dominating phase at pH 7.4 at 25 °C is Fd3m. ($b$) pure hexosomes at pH 5.0. The insert in panel b shows the corresponding intensity of the fast Fourier transform (FFT) applied to the black box region of the individual nanoparticle and the assigned Miller indices. ($c$) Dynamic light scattering (DLS) data of MO:Olalc:DOBAQ 56:41:3 mol% nanoparticles in PBS at different pH at 25 °C (green) and 37 °C (orange). At 25 °C, Fd3m micellosomes at pH 7.4 have a mean size of ~ 205 nm, whilst hexosomes are ~216 nm at pH 5; At 37 °C Fd3m micellosomes have a mean size of ~206 nm and hexosomes ~215 nm. ($d$) and ($e$) Cryo-TEM size distribution of nanoparticles hydrated at pH 7.4 and pH 5.0 respectively. Histograms were calculated from 51 nanoparticles at pH 7.4 and 40 for pH 5.0 and fitted to a Gaussian function. From the fit we obtain a mean of 65 and 132 nm for the nanoparticles at pH 7.4 and pH 5 respectively. Both DLS and Cryo-TEM data show nanoparticles at pH 5.0 generally have a slightly larger size compared to that at pH 7.4.

The particle size distribution of the nanoparticles at 25 and 37 °C was investigated using dynamic light scattering (DLS) and the results are shown in **Figure 3c**. The Fd3m micellosomes at pH 7.4 have a mean size of ~ 205 and 206 nm, whereas the hexosomes at pH 5 have a mean size of ~216

and 215 nm, at 25 and 37 °C respectively. The error bars are the mean plus the standard deviation of the average value of four different samples, each measured five times. The DLS results at 25 °C were compared with the nanoparticle size analysis from Cryo-TEM data (51 nanoparticles analyzed at pH 7.4 and 40 at pH 5.0) shown in **Figure 3d** and **3e**. The histograms were fitted to a Gaussian function and we obtain a mean size of 65 and 132 nm for the nanoparticles at pH 7.4 and pH 5, respectively. The mean size of the nanoparticles calculated differs between the two techniques, as DLS weighs the size distribution differently with larger particles emphasized as they scatter light more strongly whereas cryo-TEM often excludes larger particles from the thin ice films, emphasizing smaller particles in these polydisperse populations. Nonetheless, there is a clear trend that hexosomes are larger than the micellar cubosomes. This is because a decrease in pH leads to protonation of the DOBAQ headgroup resulting in a repulsive force at the lipid-water interface which pushes the elongation of the Fd3m micellar 'pockets' to form a tubular structure in the $H_{II}$ phase and an overall increase in the water concentration. However, the overall increase in water volume is only about 6% when hexosomes are formed, which would only account for a 2% increase in particle size (for estimations please see **Supporting information** Section 1), thus this cannot be the only explanation for the more strongly differing particle sizes. On a mesoscopic level though, there is an unneglectable difference. While the micellosomes are spherical in shape and hence display a maximized volume to surface ratio, hexosomes are by no means perfectly spherical. They display different shapes, like flat hexagonal prisms (**Figure 3b**), and often possess even "spinning top-like" structures.[43] In any case, their shape deviates significantly from that of a sphere, and hence, the apparent mean hydrodynamic size of hexosomes is bigger, whilst their volume has not increased by much. This apparent size increase of hexosomes is even more

pronounced in our cryo-TEM measurements, since we measured the diameter of the hexagonal prism section, whilst not considering the perpendicular short extension of the hexosomes.

Traditionally, cryo-TEM cannot be used to unambiguously determine the space group of lyotropic liquid crystalline phases due to the low resolution of the images leading to only a couple of peaks to be observed after applying a fast Fourier transform to the image.[44] However, it is a powerful complementary technique to SAXS. Whilst cubosomes based on bicontinuous cubic phases, and hexosomes are easier to visualize with cryo-TEM and give rise to a number of peaks in their FFTs,[45-46] cryo-TEM images of Fd3m micellosomes reported to date in the literature are of very low resolution, which is insufficient for the visualization of the internal nanostructure of the phase.

Here we have been able to obtain high resolution images and directly visualize the internal structure of the Fd3m nanoparticles along two viewing orientations, which allow us to resolve the large and small micelles of the Fd3m structure and calculate structural information using cryo-TEM for the first time.

**Figure 4** shows detailed images of Fd3m nanoparticles in two different orientations, image analysis, indexing and simulated TEM diffraction patterns. **Figure 4a** highlights an Fd3m micellosome along the [110] viewing direction with respect to the electron beam. The simulated TEM diffraction pattern from an Fd3m phase diffraction pattern viewed down the (110) plane normal (**Figure 4b**) is in excellent agreement with the experimentally determined FFT pattern. **Figure 4c** shows the FFT from the image in **Figure 4a** in which the √3, √8, √11 and √12 reflections, corresponding to Miller planes (111), (220), (311) and (222) can be clearly observed. Each theoretical reflection from the simulated diffraction pattern indexed in **Figure 4b**

corresponds to the same reflection in **Figure 4c**. The lattice parameter of the nanoparticle in **Figure 4a** was determined to be 149.3 Å (see also **Supporting Information** Section 2 for additional information on determining the lattice parameter).

**Figure 4e** shows an Fd3m nanoparticle aligned along the [114] direction with respect to the electron beam in which the √8, √11, √27 and √32 reflections, corresponding to Miller planes (220), (311), (511) and (440) were observed. Each theoretical reflection from an Fd3m phase viewed down the (114) plane normal and indexed in **Figure 4f** directly matches the experimentally determined reflections in **Figure 4g**. The lattice parameter of the particle in **Figure 4e** was determined to be 137.0 Å based on the FFT analysis.

The lattice parameters of the individual nanoparticles calculated from the cryo-TEM data are slightly different to those obtained by SAXS, which is expected, as SAXS gives the average lattice parameter of all the nanoparticles in the measured sample whilst we focus on specific nanoparticles for the cryo-TEM analysis. Based on the cryo-TEM images collected, we observe that generally nanoparticles which have a smaller lattice parameter tend to be larger in size. This finding supports our hypothesis that smaller Fd3m nanoparticles undergo a faster structural transition compared to larger particles, as they are expected to contain relatively more defects (cp. discussion above) and are thus less stable.

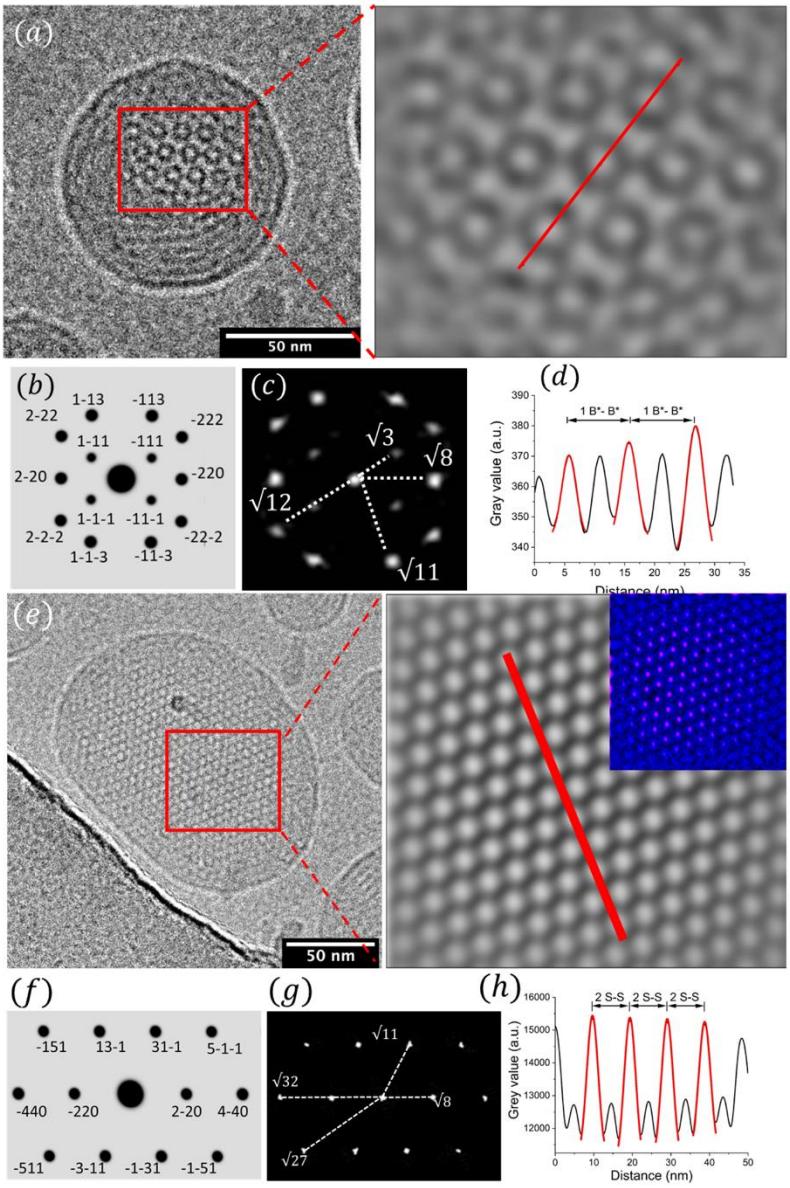


403

404 **Figure 4.** High resolution cryo-TEM images allow direct visualization of the internal structure of
405 the Fd3m nanoparticles. (*a*) Cryo-TEM image on an Fd3m micellosome of MO:Olalc:DOBAQ
406 56:41:3 mol% prepared at 25 °C and pH 7.4.The nanoparticle is aligned along the [110] orientation
407 with respect to the electron beam. The red box indicates the region used to apply the FFT shown
408 in 4c and the zoomed-in region on the right hand side shows the inverse FFT of 4c (after application
409 of rolling background subtraction and Gaussian blur), and was used to determine the $d_{B^*-B^*}$
410 distance indicated by the red line. (b) Simulated transmission electron microscopy (TEM)
411 diffraction pattern viewed down the (110) plane normal of an Fd3m phase with assigned Miller
412 indices and (c) the corresponding intensity of the FFT applied to the red box region of 4a which is
413 in excellent agreement with the simulated pattern. Each theoretical reflection from the simulated
414 pattern indexed in 4b corresponds to the same reflection in 4c. (d) Gaussian fitting of the intensity
415 profile along the red line of the inverse FFT, shown in the zoomed in region of 4a, gave an average

distance between two interval big micelles ($d_{B^*-B^*}$) of 105.5 Å. The lattice parameter of the nanoparticle in 4a was determined to be 149.3 Å, which gives a theoretical $d_{B^*-B^*}$ value of 105.5 Å. (e) cryo-TEM image of an Fd3m nanoparticle aligned along the [114] orientation with respect to the electron beam. The red box indicates the region used to apply the FFT shown in 4g and the zoomed-in region on the right hand side shows the inverse FFT of 4g (after application of rolling background subtraction and Gaussian blur), and was used to determine the $d_{S-S}$ distance indicated by the red line. The inset shows the overlay of the raw image of 4e on the left shown in blue and the inverse FFT on the right shown in magenta which are in excellent agreement. (f) Simulated transmission electron microscopy (TEM) diffraction pattern viewed down the (114) plane normal of an Fd3m phase with assigned Miller indices and (g) the corresponding intensity of the FFT applied to the red box region of 4e which is in excellent agreement with the simulated pattern. Each theoretical reflection from the simulated pattern indexed in 4f corresponds to the same reflection in 4g. (h) Gaussian fitting of the intensity profile along the red line of the inverse FFT, shown in the zoomed in region of 4e, gave an average plane to plane distance of the small micelles ($d_{S-S}$) of 48.5 Å. The lattice parameter of the nanoparticle in 8a was determined to be 137 Å, which gives a theoretical $d_{S-S}$ value of 48.4 Å.

The high resolution cryo-TEM images have allowed us to direct visualize the large and small micelles of the Fd3m structure (eight large and sixteen small micelles per unit cell), determine the micelle positions and compare them to theoretical distances for the Fd3m structure.

From geometry,[47] the big (B) micelle-to-micelle distance is given by equation 2:

$$d_{B-B} = \frac{\sqrt{3}}{4}\, a \qquad (2)$$

and the small (S) micelle-to-micelle distance is given by:

$$d_{S-S} = \frac{\sqrt{2}}{4}\, a \qquad (3)$$

**Figure 4a** shows an Fd3m micellosome aligned along the [110] orientation. The distribution of the different micelles along the (110) section will depend on where the section cuts through the plane along the z direction. Here only the big micelles are seen, however this does not represent the $d_{B-B}$ micelle-to-micelle distance defined above which is the smallest distance between two adjacent big micelles, but instead what we define as the $d_{B*-B*}$ distance, which is the distance

between two interval big micelles (i.e. two *next nearest* big micelles, see B*-B* distance in figure **S3b**) and is given by equation 4 (see also **Supporting Information** Section 3):

$$d_{B*-B*} = 2d_{S-S} = \sqrt{(\frac{8}{3})}d_{B-B} = \frac{\sqrt{2}}{2}a_{Fd3m} \quad (4)$$

Further discussion on determining the $d_{B*-B*}$ distance as well as comparing the excellent agreement of the inverse FFT (**Figure S3a**) obtained from **Figure 4c** with some 2-D serial sections of the 3-D electron density map from a previously published DOPC:DOG 1:2 mol% system adopting an Fd3m phase (**Figures S3b** and **S3c**)[42] can be found in **Supporting Information** Section 3.

Experimentally, the B*-B* distance was determined by taking the inverse FFT of **Figure 4c**, which has been background subtracted. The resulting, Gaussian blurred, inverse FFT shown on the right of **Figure 4a** was used to determine the B*-B* ($d_{B*-B*}$) distance by Gaussian fitting (**Figure 4d**) of its intensity profile along the red line in **Figure 4a** (right). The average $d_{B*-B*}$ distance measured was 105.5 Å which is identical to the theoretical distance of 105.5 Å based on the experimentally determined lattice parameter of 149.3 Å (equation 4).

**Figure 4e** shows an Fd3m micellosome aligned along the [114] orientation and highlights the small micelles of the Fd3m phase. Based on the reflections of the FFT in **Figure 4g**, the lattice parameter was determined to be 137 Å, which gives a theoretical $d_{S-S}$ micelle-to-micelle distance of 48.4 Å (equation 2). Note the √8 refection also corresponds to the S-S micelle distance. The $d_{S-S}$ distance was determined by taking the inverse FFT of **Figure 4g**, which has been background subtracted. The resulting, Gaussian blurred, inverse FFT is shown in **Figure 4e** (right) was used to determine the $d_{S-S}$ distance by Gaussian fitting (**Figure 4h**) of its intensity profile along the red line in **Figure 4e** (right). The overlay of the raw image of **Figure 4e** (left) shown in blue and

inverse FFT (from **Figure 4g**) shown in magenta are in excellent agreement (**Figure 4a,** right, inset). It should be noted that in the [114] direction, $d_{S-S}$ does not correspond to the distance between two adjacent small micelles as shown in **Figure S3b** for the (110) section but is instead the plane to plane distance of the small micelles in this projection (**Figure 4e** (right), see also **Figure S4**). The experimentally determined S-S plane distance (**Figure 4h**) and the (220) reflection from **Figure 4g** were 48.5 and 48.3 Å respectively and match the theoretical distance of 48.4 Å determined above.

## CONCLUSION

We have been able to generate highly sensitive pH responsive lyotropic liquid crystalline nanoparticles that require only a very small amount (3 mol%) of pH sensitive lipid to switch between a compartmentalized internal structure based on space group Fd3m at physiological pH to an accessible porous 2D hexagonal structure when the pH is ≤6 at both 25 and 37 °C. The transition is fully reversible by tuning the inverse spontaneous curvature by the protonation or deprotonation of the pH sensitive lipid's headgroup. The internal symmetry of the nanoparticles was confirmed by SAXS and cryo-TEM. Imaging of Fd3m nanoparticles has been challenging with cryo-TEM however we have managed to acquire high resolution images of them and directly visualize the structure in unprecedented detail for the first time. Depending on the direction the particles are aligned with respect to the electron beam we can resolve the large and small inverse micelles of the Fd3m phase which allowed us to calculate structural information such as the positions and distances of the two different sized micelles and compare these to theory based on geometrical considerations. These promising findings could pave the way to developing superior stimuli-responsive soft nanoparticle formulations that change their connectivity upon encountering

acidic pH, which is known for example to be highly important both in human disease as well as plant physiology and crop performance. They can potentially benefit a range of downstream applications in the biomedical, food, agrochemical and environmental remediation industries.

## EXPERIMENTAL SECTION

**Preparation of MO/Olalc/DOBAQ nanoparticles**. Monoolein (MO; was a kind gift from Croda Personal Care, Goole, UK), Oleyl alcohol (Olalc; Sigma Aldrich, Gillingham, UK), N-(4-carboxybenzyl)-N,N-dimethyl-2,3-bis(oleoyloxy)propan-1-aminium (DOBAQ; Avanti polar lipids, AL, USA) were weighted and dissolved in chloroform (Sigma-Aldrich, Gillingham, UK), then mixed at the desired MO:Olalc:DOBAQ molar ratios. MO had a purity of >92% (containing a minimum of 92% monoester and maximum 8% diester) whilst the rest of the lipids had a purity of >99% and were used without further purification. The chloroform solutions were dried using a stream of $N_2$ gas and the dry thin films were left under vacuum overnight to remove any residual organic solvent. Thin films were then heated to 60 °C and hydrated with phosphate-buffered saline buffer (PBS; Sigma-Aldrich, Gillingham, UK) containing 6.923 mg/ml Pluronic F127, 5 wt% F127 of total lipids, (Sigma-Aldrich, Gillingham, U.K.) to achieve a sample concentration of 100 mg/ml. Dispersed samples were prepared by tip sonication (VibraCell 750 with a stepped microtip, Sonics & Materials Inc, Newtown, USA) for 30 minutes in pulse mode (1s pulse, 1s break) at 35% of its maximum power (750 W). The pH of the NP dispersions was readjusted to 7.4 using 0.1M NaOH (Fisher Scientific, Loughborough, UK) or 0.1M HCl (Fisher Scientific, Loughborough, U.K.). Samples for SAXS measurements were measured after the pH was switched under two conditions: 1) immediately after switching and 2) after equilibration at 37 °C overnight. SAXS patterns of samples under condition 1 were collected at 37 °C whereas samples SAXS patterns for

samples under condition 2 were collected at both 25 and 37 °C. The pH of the dispersed nanoparticles was first gradually decreased from 7.4 to 3.0, then increased back to 7.4 while taking out samples at each selected pH point for SAXS measurements at both 25 °C and 37 °C. For the dynamic light scattering and cryogenic transmission electron microscopy data, lipid nanoparticles were hydrated by PBS at pH 7.4 or pH 5.0 directly and allowed to equilibrate overnight at 37 °C before measurement.

**Synchrotron Small-Angle X-ray Scattering (SAXS).** Synchrotron SAXS data were collected on beamline I22 at Diamond Light Source. The synchrotron X-ray beam was set to 18 keV which corresponds to a wavelength of 0.69 Å. The sample to detector distance was set at 6 or 8.7 m and the 2-D powder diffraction patterns were recorded on a Pilatus 2M detector. SAXS data were analyzed using the DAWN software.[48-49] The lattice parameters of the Fd3m and $H_{II}$ phases were calculated using the equations below:

$$a_{Fd3m} = \frac{2\pi}{q_{hkl}}\sqrt{h^2 + k^2 + l^2} \quad (5)$$

$$a_{H_{II}} = \frac{4\pi}{\sqrt{3}\, q_{hk}}\sqrt{h^2 + k^2 + hk} \quad (6)$$

where $q_{hkl}$ or $q_{hk}$ is the scattering vector and $hkl$ or $hk$ are the Miller indices of a given Bragg peak. Samples were equilibrated at 25 °C and 37 °C for 5 min before taking measurements.

**Dynamic Light Scattering (DLS).** For DLS measurements, particles were made at a concentration of 5 mg/mL. In total, four different samples were measured and each sample was measured five times. Samples were diluted to 25 μg/mL by isotonic PBS at different pH before

DLS measurement. The mean hydrodynamic radius and polydispersity index width (PDI) of the nanoparticles were measured at pH 7.4 and pH 5.0 using a Malvern Zetasizer Nano ZSP instrument (Malvern Panalytical, Malvern, UK) equipped with a 633 nm helium-neon laser. Samples were measured at 25 °C or 37 °C at a fixed 173° backscattering angle. The refractive index and absorption of the nanoparticles was set as 1.46 and 0.001 respectively using values for pure MO. The refractive index of PBS is 1.334 and its viscosity was set to 0.9110 mPa.s at 25 °C and 0.7130 mPa.s at 37 °C.

**Cryogenic-transmission electron microscopy (Cryo-TEM).** Samples were diluted once (final concentration of 50 mg/ml) in isotonic PBS at the required pH for the morphological characterization using cryo-TEM. In brief, 3 µL of the diluted sample was applied to freshly glow discharged Cu QUANTIFOIL grids (R2/R2, 300 or 400 mesh) with a hold time of 30 s. The carbon-coated grids were glow discharged at 10 mA for 20 s for samples at pH 7.4 and 30 s for samples at pH 5.0. The grids were blotted for 6 s with a blotting force of 7 at 25 °C under 100% relatively humidity, then plunged into liquid ethane using a Vitrobot™ mark IV (Thermo/FEI). Grids were kept under liquid nitrogen before measurement.

Data acquisition was carried out on a Titan KRIOS microscope (Thermo Fisher Scientific, US) with an accelerating voltage of 300 kV and a defocus value of -1 µm at a nominal magnification of 45k or 75k. The pixel size for these images were 1.76 and 1.065 Å, respectively. Image processing was done using Fiji.[50] The Fast Fourier Transforms (FFTs) of the raw images were background subtracted. The d-spacing of each reflection in the FFT was determined using TrackMate.[51] The micelle distances were calculated from the inverse FFTs after application of rolling background subtraction and Gaussian blur using Fiji.

**Simulation of TEM diffraction patterns.** The program CrystalMaker® (CrystalMaker Software Ltd, Oxford, England-www.crystalmaker.com) was used to visualize 2-D sections (110 and 114 planes) through the model structure of the Fd3m cubic phase. Fd3m origin 2 (at $\bar{3}m$) was used. These sections were then sent to the SingleCrystal™ program to simulate transmission electron microscopy (TEM) diffraction patterns.

ASSOCIATED CONTENT

**Supporting Information**

Discussion on the estimation of micellosome and hexosome size ratios, details on the calculation of lattice parameters from cryo-TEM data and determination of the micelle positions in Fd3m nanoparticles. This material is available free of charge via the Internet at http://pubs.acs.org.

**AUTHOR INFORMATION**

**Corresponding Author**

**Arwen I.I. Tyler -** School of Food Science and Nutrition, University of Leeds, Leeds, LS2 9JT, United Kingdom

Email: A.I.I.Tyler@leeds.ac.uk

**Authors**

**Zexi Xu** - School of Food Science and Nutrition and School of Chemistry, University of Leeds, Leeds, LS2 9JT, United Kingdom

**John M. Seddon** - Department of Chemistry, Imperial College London, London, W12 0BZ, United Kingdom.

**Michael Rappolt** - School of Food Science and Nutrition, University of Leeds, Leeds, LS2 9JT, United Kingdom.

**Paul A. Beales** - School of Chemistry and Astbury Centre for Structural Molecular Biology, University of Leeds, Leeds, LS2 9JT, United Kingdom

## Author Contributions

A.I.I.T. conceived and designed the experiments. J.M.S, P.A.B., M.R. and A.I.I.T contributed to study design. Z.X. performed all the experiments. Z.X., M.R. and A.I.I.T. analyzed the data. Z.X., P.A.B., M.R. and A.I.I.T. interpreted the results. Z.X. M.R. and A.I.I.T co-wrote the manuscript. All authors discussed the results and commented on the manuscript.

## Funding Sources

The research was supported by start-up funding awarded to A.I.I.T. from the University of Leeds as a well as a PhD scholarship awarded to Z.X.

## Notes

The authors declare no competing financial interest.

## ACKNOWLEDGMENTS

We thank Diamond Light Source for the award of synchrotron beamtimes (SM18027-1, SM22659-1 and SM24530-1) as well as Dr. Andy Smith, Dr. Tim Snow and Professor Nick Terrill for their support and assistance. We thank Dr. Aleks Ponjavic from the University of Leeds for help with

some aspects of image processing and analysis and drawing figures. We also thank Dr. Rebecca Thompson from the Astbury Biostructure Facility and Rashmi Seneviratne from the School of Chemistry at the University of Leeds for their support with Cryo-TEM. The FEI Titan Krios microscope used was funded by the University of Leeds (UoL ABSL award) and Wellcome Trust (108466/Z/15/Z). The Bragg Centre for Materials Research at the University of Leeds is also acknowledged.

## References

1. Nguyen, T. H.; Hanley, T.; Porter, C. J.; Boyd, B. J., Nanostructured liquid crystalline particles provide long duration sustained-release effect for a poorly water soluble drug after oral administration. *J Control Release* **2011,** *153* (2), 180-186.
2. Kim, H.; Leal, C., Cuboplexes: Topologically Active siRNA Delivery. *ACS Nano* **2015,** *9* (10), 10214-10226.
3. Praca, F. S. G.; Medina, W. S. G.; Petrilli, R.; Bentley, M. V. L. B., Liquid Crystal Nanodispersions Enable the Cutaneous Delivery of Photosensitizer for Topical PDT: Fluorescence Microscopy Study of Skin Penetration. *Current Nanoscience* **2012,** *8* (4), 535-540.
4. Jain, V.; Swarnakar, N. K.; Mishra, P. R.; Verma, A.; Kaul, A.; Mishra, A. K.; Jain, N. K., Paclitaxel loaded PEGylated gleceryl monooleate based nanoparticulate carriers in chemotherapy. *Biomaterials* **2012,** *33* (29), 7206-7220.
5. Rizwan, S. B.; McBurney, W. T.; Young, K.; Hanley, T.; Boyd, B. J.; Rades, T.; Hook, S., Cubosomes containing the adjuvants imiquimod and monophosphoryl lipid A stimulate robust cellular and humoral immune responses. *J Control Release* **2013,** *165* (1), 16-21.
6. Zhai, J.; Fong, C.; Tran, N.; Drummond, C. J., Non-Lamellar Lyotropic Liquid Crystalline Lipid Nanoparticles for the Next Generation of Nanomedicine. *ACS Nano* **2019,** *13* (6), 6178-6206.
7. Ganta, S.; Devalapally, H.; Shahiwala, A.; Amiji, M., A review of stimuli-responsive nanocarriers for drug and gene delivery. *J Control Release* **2008,** *126* (3), 187-204.
8. Warburg, O., On the origin of cancer cells. *Science* **1956,** *123* (3191), 309-314.
9. Hrubý, M.; Koňák, Č.; Ulbrich, K., Polymeric micellar pH-sensitive drug delivery system for doxorubicin. *Journal of Controlled Release* **2005,** *103* (1), 137-148.
10. Fong, W. K.; Negrini, R.; Vallooran, J. J.; Mezzenga, R.; Boyd, B. J., Responsive self-assembled nanostructured lipid systems for drug delivery and diagnostics. *J Colloid Interface Sci* **2016,** *484*, 320-339.
11. Boelsma, E.; van de Vijver, L. P.; Goldbohm, R. A.; Klöpping-Ketelaars, I. A.; Hendriks, H. F.; Roza, L., Human skin condition and its associations with nutrient concentrations in serum and diet. *The American journal of clinical nutrition* **2003,** *77* (2), 348-355.

12. Cederberg, C.; Rohss, K.; Lundborg, P.; Olbe, L., Effect of once daily intravenous and oral omeprazole on 24-hour intragastric acidity in healthy subjects. *Scand J Gastroenterol* **1993,** *28* (2), 179-184.
13. Hu, Y.-B.; Dammer, E. B.; Ren, R.-J.; Wang, G., The endosomal-lysosomal system: from acidification and cargo sorting to neurodegeneration. *Translational Neurodegeneration* **2015,** *4* (1), 18.
14. Sorkin, A.; Von Zastrow, M., Signal transduction and endocytosis: close encounters of many kinds. *Nat Rev Mol Cell Biol* **2002,** *3* (8), 600-614.
15. Kocak, G.; Tuncer, C.; Bütün, V., pH-Responsive polymers. *Polymer Chemistry* **2017,** *8* (1), 144-176.
16. Deirram, N.; Zhang, C.; Kermaniyan, S. S.; Johnston, A. P. R.; Such, G. K., pH-Responsive Polymer Nanoparticles for Drug Delivery. *Macromolecular Rapid Communications* **2019,** *40* (10), 1800917.
17. Mezzenga, R.; Seddon, J. M.; Drummond, C. J.; Boyd, B. J.; Schröder-Turk, G. E.; Sagalowicz, L., Nature-Inspired Design and Application of Lipidic Lyotropic Liquid Crystals. *Advanced Materials* **2019,** *31* (35), 1900818.
18. Tan, A.; Hong, L.; Du, J. D.; Boyd, B. J., Self-Assembled Nanostructured Lipid Systems: Is There a Link between Structure and Cytotoxicity? *Advanced Science* **2019,** *6* (3), 1801223.
19. Luzzati, V.; Husson, F., The structure of the liquid-crystalline phasis of lipid-water systems. *J Cell Biol* **1962,** *12*, 207-219.
20. Luzzati, V.; Reiss-Husson, F., Structure of the Cubic Phase of Lipid-Water Systems. *Nature* **1966,** *210* (5043), 1351-1352.
21. Seddon, J. M., Structure of the inverted hexagonal (HII) phase, and non-lamellar phase transitions of lipids. *Biochim Biophys Acta* **1990,** *1031* (1), 1-69.
22. Kaasgaard, T.; Drummond, C. J., Ordered 2-D and 3-D nanostructured amphiphile self-assembly materials stable in excess solvent. *Physical Chemistry Chemical Physics* **2006,** *8* (43), 4957-4975.
23. Guillot, S.; Moitzi, C.; Salentinig, S.; Sagalowicz, L.; Leser, M. E.; Glatter, O., Direct and indirect thermal transitions from hexosomes to emulsified micro-emulsions in oil-loaded monoglyceride-based particles. *Colloids and Surfaces A: Physicochemical and Engineering Aspects* **2006,** *291* (1), 78-84.
24. Yaghmur, A.; de Campo, L.; Salentinig, S.; Sagalowicz, L.; Leser, M. E.; Glatter, O., Oil-loaded monolinolein-based particles with confined inverse discontinuous cubic structure (Fd3m). *Langmuir* **2006,** *22* (2), 517-521.
25. Yaghmur, A.; de Campo, L.; Sagalowicz, L.; Leser, M. E.; Glatter, O., Emulsified microemulsions and oil-containing liquid crystalline phases. *Langmuir* **2005,** *21* (2), 569-577.
26. Boyd, B. J.; Whittaker, D. V.; Khoo, S.-M.; Davey, G., Lyotropic liquid crystalline phases formed from glycerate surfactants as sustained release drug delivery systems. *International Journal of Pharmaceutics* **2006,** *309* (1), 218-226.
27. Phan, S.; Fong, W.-K.; Kirby, N.; Hanley, T.; Boyd, B. J., Evaluating the link between self-assembled mesophase structure and drug release. *International Journal of Pharmaceutics* **2011,** *421* (1), 176-182.
28. Negrini, R.; Mezzenga, R., pH-responsive lyotropic liquid crystals for controlled drug delivery. *Langmuir* **2011,** *27* (9), 5296-5303.

29. Negrini, R.; Fong, W.-K.; Boyd, B. J.; Mezzenga, R., pH-responsive lyotropic liquid crystals and their potential therapeutic role in cancer treatment. *Chemical Communications* **2015,** *51* (30), 6671-6674.
30. Oka, T.; Tsuboi, T.-a.; Saiki, T.; Takahashi, T.; Alam, J. M.; Yamazaki, M., Initial Step of pH-Jump-Induced Lamellar to Bicontinuous Cubic Phase Transition in Dioleoylphosphatidylserine/Monoolein. *Langmuir* **2014,** *30* (27), 8131-8140.
31. Salentinig, S.; Sagalowicz, L.; Glatter, O., Self-assembled structures and pKa value of oleic acid in systems of biological relevance. *Langmuir* **2010,** *26* (14), 11670-11679.
32. Gontsarik, M.; Mohammadtaheri, M.; Yaghmur, A.; Salentinig, S., pH-Triggered nanostructural transformations in antimicrobial peptide/oleic acid self-assemblies. *Biomater Sci* **2018,** *6* (4), 803-812.
33. Fong, C.; Zhai, J.; Drummond, C. J.; Tran, N., Micellar Fd3m cubosomes from monoolein – long chain unsaturated fatty acid mixtures: Stability on temperature and pH response. *Journal of Colloid and Interface Science* **2020,** *566*, 98-106.
34. Kulkarni, C. V.; Tang, T.-Y.; Seddon, A. M.; Seddon, J. M.; Ces, O.; Templer, R. H., Engineering bicontinuous cubic structures at the nanoscale—the role of chain splay. *Soft Matter* **2010,** *6* (14), 3191-3194.
35. Briggs, J.; Chung, H.; Caffrey, M., The Temperature-Composition Phase Diagram and Mesophase Structure Characterization of Monoolein/Water System. *Journal de Physique II* **1996,** *6* (5), 723-751.
36. Walsh, C. L.; Nguyen, J.; Szoka, F. C., Synthesis and characterization of novel zwitterionic lipids with pH-responsive biophysical properties. *Chemical Communications* **2012,** *48* (45), 5575-5577.
37. Nakano, M.; Teshigawara, T.; Sugita, A.; Leesajakul, W.; Taniguchi, A.; Kamo, T.; Matsuoka, H.; Handa, T., Dispersions of Liquid Crystalline Phases of the Monoolein/Oleic Acid/Pluronic F127 System. *Langmuir* **2002,** *18* (24), 9283-9288.
38. Kollmitzer, B.; Heftberger, P.; Rappolt, M.; Pabst, G., Monolayer spontaneous curvature of raft-forming membrane lipids. *Soft Matter* **2013,** *9* (45), 10877-10884.
39. Tyler, A. I.; Barriga, H. M.; Parsons, E. S.; McCarthy, N. L.; Ces, O.; Law, R. V.; Seddon, J. M.; Brooks, N. J., Electrostatic swelling of bicontinuous cubic lipid phases. *Soft Matter* **2015,** *11* (16), 3279-3286.
40. Caboi, F.; Amico, G. S.; Pitzalis, P.; Monduzzi, M.; Nylander, T.; Larsson, K., Addition of hydrophilic and lipophilic compounds of biological relevance to the monoolein/water system. I. Phase behavior. *Chemistry and Physics of Lipids* **2001,** *109* (1), 47-62.
41. Dong, Y.-D.; Tilley, A. J.; Larson, I.; Lawrence, M. J.; Amenitsch, H.; Rappolt, M.; Hanley, T.; Boyd, B. J., Nonequilibrium Effects in Self-Assembled Mesophase Materials: Unexpected Supercooling Effects for Cubosomes and Hexosomes. *Langmuir* **2010,** *26* (11), 9000-9010.
42. Tyler, A. I.; Shearman, G. C.; Brooks, N. J.; Delacroix, H.; Law, R. V.; Templer, R. H.; Ces, O.; Seddon, J. M., Hydrostatic pressure effects on a hydrated lipid inverse micellar Fd3m cubic phase. *Phys Chem Chem Phys* **2011,** *13* (8), 3033-3038.
43. Boyd, B. J.; Rizwan, S. B.; Dong, Y.-D.; Hook, S.; Rades, T., Self-Assembled Geometric Liquid-Crystalline Nanoparticles Imaged in Three Dimensions: Hexosomes Are Not Necessarily Flat Hexagonal Prisms. *Langmuir* **2007,** *23* (25), 12461-12464.

44. Sagalowicz, L.; Acquistapace, S.; Watzke, H. J.; Michel, M., Study of Liquid Crystal Space Groups Using Controlled Tilting with Cryogenic Transmission Electron Microscopy. *Langmuir* **2007,** *23* (24), 12003-12009.
45. Barauskas, J.; Johnsson, M.; Tiberg, F., Self-assembled lipid superstructures: beyond vesicles and liposomes. *Nano Lett* **2005,** *5* (8), 1615-1619.
46. Demurtas, D.; Guichard, P.; Martiel, I.; Mezzenga, R.; Hebert, C.; Sagalowicz, L., Direct visualization of dispersed lipid bicontinuous cubic phases by cryo-electron tomography. *Nat Commun* **2015,** *6*, 8915.
47. Duesing, P. M.; Templer, R. H.; Seddon, J. M., Quantifying Packing Frustration Energy in Inverse Lyotropic Mesophases. *Langmuir* **1997,** *13* (2), 351-359.
48. Basham, M.; Filik, J.; Wharmby, M. T.; Chang, P. C.; El Kassaby, B.; Gerring, M.; Aishima, J.; Levik, K.; Pulford, B. C.; Sikharulidze, I.; Sneddon, D.; Webber, M.; Dhesi, S. S.; Maccherozzi, F.; Svensson, O.; Brockhauser, S.; Naray, G.; Ashton, A. W., Data Analysis WorkbeNch (DAWN). *J Synchrotron Radiat* **2015,** *22* (3), 853-858.
49. Filik, J.; Ashton, A. W.; Chang, P. C. Y.; Chater, P. A.; Day, S. J.; Drakopoulos, M.; Gerring, M. W.; Hart, M. L.; Magdysyuk, O. V.; Michalik, S.; Smith, A.; Tang, C. C.; Terrill, N. J.; Wharmby, M. T.; Wilhelm, H., Processing two-dimensional X-ray diffraction and small-angle scattering data in DAWN 2. *Journal of applied crystallography* **2017,** *50* (Pt 3), 959-966.
50. Schindelin, J.; Arganda-Carreras, I.; Frise, E.; Kaynig, V.; Longair, M.; Pietzsch, T.; Preibisch, S.; Rueden, C.; Saalfeld, S.; Schmid, B.; Tinevez, J. Y.; White, D. J.; Hartenstein, V.; Eliceiri, K.; Tomancak, P.; Cardona, A., Fiji: an open-source platform for biological-image analysis. *Nat Methods* **2012,** *9* (7), 676-682.
51. Tinevez, J. Y.; Perry, N.; Schindelin, J.; Hoopes, G. M.; Reynolds, G. D.; Laplantine, E.; Bednarek, S. Y.; Shorte, S. L.; Eliceiri, K. W., TrackMate: An open and extensible platform for single-particle tracking. *Methods* **2017,** *115*, 80-90.